Influence of magnetism on Dirac semimetallic behavior in nonstoichiometric $Sr_{1-y}Mn_{1-z}Sb_2$ ($y \sim 0.07, z \sim 0.02$)

Qiang Zhang,[1,2,*] Satoshi Okamoto,[3,†] Matthew B. Stone,[2] Jinyu Liu,[4] Yanglin Zhu,[4] John DiTusa,[1] Zhiqiang Mao,[4,5] and David Alan Tennant[3,6,‡]

[1]*Department of Physics and Astronomy, Louisiana State University, Baton Rouge, Louisiana 70803, USA*
[2]*Neutron Scattering Division, Oak Ridge National Laboratory, Oak Ridge, Tennessee 37831, USA*
[3]*Materials Science and Technology Division, Oak Ridge National Laboratory, Oak Ridge, Tennessee 37831, USA*
[4]*Department of Physics and Engineering Physics, Tulane University, New Orleans, Louisiana 70118, USA*
[5]*Department of Physics, Pennsylvania State University, University Park, Pennsylvania 16802, USA*
[6]*Shull Wollan Center, Oak Ridge National Laboratory, Oak Ridge, Tennessee 37831, USA*

(Received 6 January 2019; revised manuscript received 15 October 2019; published 5 November 2019)

Nonstoichiometric $Sr_{1-y}Mn_{1-z}Sb_2$ ($y, z < 0.1$) is known to exhibit a coexistence of magnetic order and the nontrivial semimetallic behavior. In this paper, we report the magnetism and its strong coupling to the semimetallic behavior, by a combined use of inelastic neutron scattering (INS) and density functional theory (DFT). A phase separation consisting of a majority antiferromagentic phase and a minority ferromagnetic phase is proposed. We found a relatively large spin excitation gap ≈8.5 meV at 5 K, and the interlayer magnetic exchange constant only 2.8% of the dominant intralayer magnetic interaction, evidencing a quasi-2D magnetism in $Sr_{1-y}Mn_{1-z}Sb_2$. Using DFT, we find a strong influence of magnetic orders on the electronic band structure and the Dirac dispersions near the Fermi level along the Y-S direction in the presence of a ferromagnetic order. Furthermore, we demonstrate that the size of the ferromagnetic ordered moment is an effective strategy to tune Dirac/Weyl dispersions near the Fermi level. Our study unveils novel interplay between the magnetic order, ordered moment, and electronic band topology in $Sr_{1-y}Mn_{1-z}Sb_2$ and opens pathways to control the relativistic band structure.

DOI: 10.1103/PhysRevB.100.205105

I. INTRODUCTION

Topological semimetals [1,2] are a newly emerged frontier in condensed matter physics and have stimulated tremendous research interest because they give access to new quantum phenomena and are very attractive for both fundamental research and technological application. Particular attention has focused on Weyl or Dirac semimetals that exhibit a coexistence with magnetism as a promising route to modify and control Weyl/Dirac fermions, electronic transport properties, and band topology. Among them, $SrMnSb_2$ has attracted intense interest very recently and its topological semimetal behavior is hotly debated. Liu *et al.* [3] reported a nontrivial semimetallic behavior related to Dirac or Weyl fermions including nearly massless quasiparticles with a π Berry phase coupled to ferromagnetism in nonstoichiometric $Sr_{1-y}Mn_{1-z}Sb_2$. For the magnetic behavior, it displays ferromagnetic (FM) order below $T_C \sim 565$ K, followed by a transition to a possible canted antiferromagnetic (AFM) order with a net FM component below $T_{\text{FM-AFM}} \approx 304$ K [3]. The nontrivial semimetal behavior was further supported by optical conductivity and ultrafast optical pump-probe measurements [4]. Nevertheless, Ramankutty *et al.* [5] reported zero Berry phase in nearly stoichiometric $SrMnSb_2$. Previous density functional theory (DFT) calculations [5–7] showed that the lattice distortion in the orthorhombic structure prevents the formation of the Dirac points near the Fermi level by opening a gap. Both results cannot account for the observed topological semimetallic behavior reported in Ref. [3]. It is therefore challenging to explore whether there are indeed Dirac/Weyl points in proximity to the Fermi level and what drives their formation in $Sr_{1-y}Mn_{1-z}Sb_2$. Furthermore, $SrMnSb_2$ offers a wonderful opportunity to address an important and general question whether there is a close correlation between magnetic order and band topology in 3D magnetic topological semimetals.

In addition to $SrMnSb_2$, other alkaline earth ternary $AMnC_2$ "112" compounds (A = Sr, Ca, Ba, C = Bi or Sb) [8–12] were reported to be Dirac semimetal candidates with the coexistence of AFM order. An interplay between magnetic order and electronic transport properties was found in $CaMnBi_2$ [13] due to coupling of the interlayer ferromagnetic component to the planar Bi electrons. The Dirac carriers in Bi layers were reported to enhance the interlayer exchange coupling $J_\perp$ significantly between magnetic layers in $AMnBi_2$ (A=Ca, Sr) by the Raman spectroscopy [14]. However, Rahn *et al.* [8] argued that the neglect of single-ion anisotropy D in the Raman analysis may significantly exaggerate the obtained interlayer magnetic coupling since D and $J_\perp$ are correlated. All of these facts emphasize the importance of an accurate

*zhangq6@ornl.gov
†okapon@ornl.gov
‡tennantda@ornl.gov

determination of the interlayer magnetic coupling and the magnetic dimensionality in "112" compounds.

Here, by a combined neutron scattering and DFT study, we report the magnetism and its coupling to the relativistic band structure in $Sr_{1-y}Mn_{1-z}Sb_2$. We argue that phase segregation into majority AFM and minority FM phases is realized at low temperatures. Focusing on the majority AFM phase, we extract the (essentially 2D) magnetic interactions from both spin-wave measurements and DFT calculations. Strikingly, the magnetic order is found to strongly affect the relativistic band structure with the FM phase that supports the nontrivial Dirac semimetal behavior in contrast to the AFM phase suppressing it significantly. Furthermore, we demonstrate how the Dirac/Weyl dispersion near the Fermi level can be tuned effectively by the size of the FM moment.

II. EXPERIMENTAL AND THEORETICAL DETAILS

$Sr_{1-y}Mn_{1-z}Sb_2$ ($y \sim 0.07$ and $z \sim 0.02$) crystals were grown using a flux technique [3]. Several single crystals with a total mass of approximately 600 mg were co-aligned at the $(0\,K\,L)$ horizontal scattering plane within ~ 3 degrees mosaicity. Inelastic neutron scattering experiments were performed using the Spallation Neutron Source's SEQUOIA spectrometer at Oak Ridge National Laboratory. The data were collected at 5 K and 350 K using a few different incident energies of 35, 70, 100, 160, 200 meV. The wave vectors **Q** reported here are defined in the reciprocal lattice unit (rlu). The constant-energy (E) cuts were fitted using a Lorentzian function to obtain both the spin wave dispersion and intensity. The fits to spin wave dispersion and intensity using the SpinW package [15] yield the magnetic exchange constants and single-ion anisotropy. DFT calculations were performed using the generalized gradient approximation and projector augmented wave approach [16] as implemented in the Vienna *ab initio* simulation package (VASP) [17,18]. For Sr, a potential, in which semicore s and p states are treated as valence states, is used (Sr_{sv}), and for Mn and Sb, standard potentials were used (Mn and Sb, respectively, in the VASP distribution). In most cases, we use a $2 \times 8 \times 8$ **k**-point grid and an E cutoff of 500 eV with spin-orbit coupling included. The $+U$ correction is not included because $SrMnSb_2$ is an itinerant magnetic system.

III. RESULTS AND DISCUSSION

Figure 1(a) shows the crystal and magnetic structures in $Sr_{1-y}Mn_{1-z}Sb_2$. It crystallizes in the orthorhombic structure with space group *Pnma* (No. 62), consisting of a MnSb layer with edge-sharing $MnSb(2)_4$ tetrahedral and a flat Sb(1) layer sandwiched between two staggered Sr planes. The two magnetic structures previously proposed [3] for $T < T_{\text{FM-AFM}}$ and $T_{\text{FM-AFM}} < T < T_C$ are illustrated in Fig. 1(a). A critical exponent $\beta \approx 0.25$ [see Fig. 1(b)] falls in the region $0.1 < \beta < 0.25$ expected for quasi-2D systems [19–21]. The AFM ordered moment is found to be $M \approx 3.77(9)\ \mu_B$, corresponding to $S \approx 1.89$ at 5 K [3]. The field dependence of the magnetization in the inset of Fig. 1(b) confirms a clear ferromagnetism below $T < T_C$ down to 5 K. Note that the low-temperature canted magnetic structure combines both

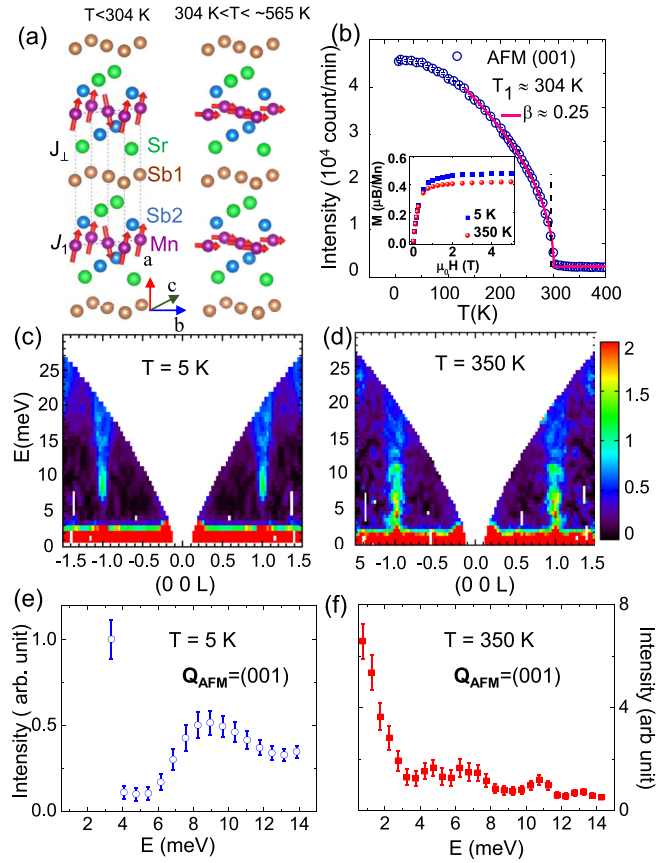

FIG. 1. (a) Magnetic structures of $Sr_{1-y}Mn_{1-z}Sb_2$ proposed previously in Ref. [3]: canted AFM order in $T < 304$ K and FM order with a moment along the b axis in 304 K $< T <\sim 565$ K. (b) Temperature dependence of the peak intensity for the pure AFM Bragg peak (001) taken from Ref. [3]. The solid line is the fit to the power law. Inset shows the field dependence of the magnetization at different temperatures. Magnetic excitations near the AFM zone center (0 0 $\pm$ 1) at (c) 5 K and (d) 350 K. The corresponding constant-Q cuts at 5 K and 350 K are shown in (e) and (f), respectively.

C-type AFM and FM components in the a and b directions, respectively. Nevertheless, they belong to different irreducible representations [3], so they are not normally expected to occur in a single phase. In addition, we will show that the interactions are strong, Heisenberg-type, and antiferromagnetic. Spin canting along the b axis would require a large effective field perpendicular to the AFM moments. The only likely source would be a Dzyaloshinskii-Moriya (DM) interaction, but the required DM vector is disallowed by lattice symmetry. We therefore propose that spatially separated C-type AFM and FM phases are forming with the measured moments implying the AFM phase is the majority fraction (around 88% by volume), which is further supported by our DFT calculations shown below.

To investigate the spin dynamics of $Sr_{1-y}Mn_{1-z}Sb_2$, we performed inelastic neutron scattering measurements. Figures 1(c) and 1(e) and Figs. 1(d) and 1(f) compare the magnetic excitations near the AFM zone center (0 0 1) at 5 K ($T < T_{\text{FM-AFM}}$) and 350 K ($T_{\text{FM-AFM}} < T < T_C$). Given the smaller volume from the FM component, inelastic neutron scattering

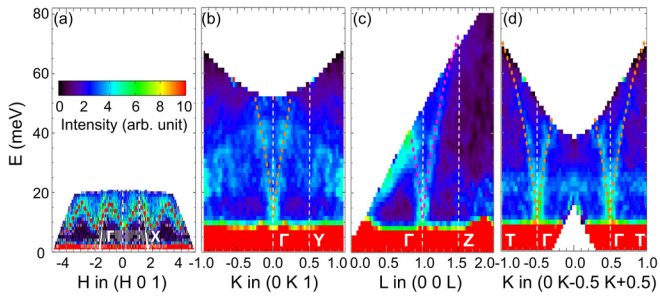

FIG. 2. Magnetic excitations near the AFM zone center (0 0 1) at 5 K, along high-symmetry directions: (a) out-of-plane H, in-plane (b) K, (c) L, and (d) diagonal [0 K K] directions. The dashed lines are fits to the experimental spin wave dispersions. The vertical lines indicate the AFM zone center or boundaries, with the Brillouin symbols marked in the figures.

primarily measures the dominant AFM signal. At 5 K within the AFM ordered state, a clear spin gap $E_g \approx 8.5$ meV is observed indicative of the existence of a single-ion anisotropy. The spin gap closes at 350 K when the long-range AFM order disappears. Furthermore, whereas the spin wave dispersion exists at 5 K, the dispersion disappears and evolves into a spin fluctuation spectra near the AFM zone centers at 350 K. The magnetic excitations along out-of-plane H, in-plane K, L, and diagonal [0 K K] directions at 5 K are displayed in Figs. 2(a)–2(d) [the high-symmetric Brillouin symbols are illustrated in the inset of Fig. 4(a)]. There is a steep dispersion along in-plane directions extending to ≈70 meV at the AFM zone boundary Z and T points, but the dispersion along out-of-plane H direction is much weaker, with $E \approx 18$ meV at the zone-boundary X point, indicating a quasi-2D magnetism.

Figure 3 compares constant-energy slices in the (0 K L) scattering plane at energy transfers around 5, 17, and 30 meV at 5 and 350 K. At 5 K, no magnetic excitations are apparent around 5 meV in Fig. 3(a) owing to the existence of higher spin gap of $E_g \approx 8.5$ meV. As the transferred E increases,

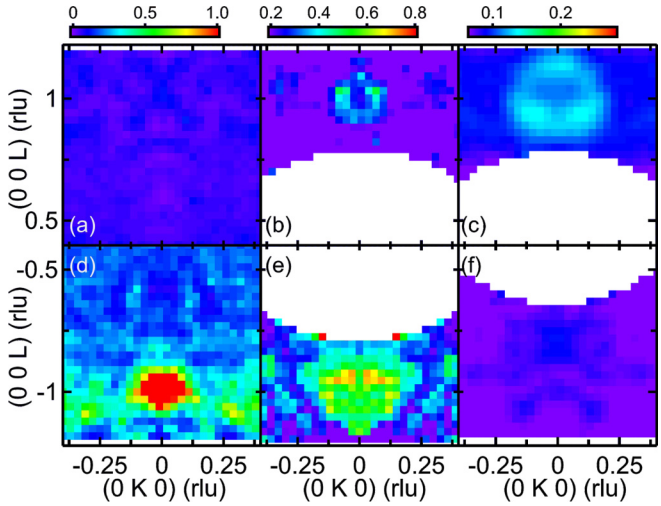

FIG. 3. Constant-E slices in the (0 K L) scattering plane around E of (a) 5 meV, (b) 17 meV, and (c) 30 meV at 5 K. Corresponding constant-E slices at 350 K are shown in (d)–(f).

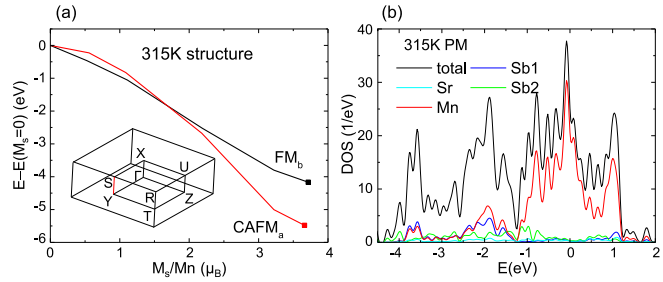

FIG. 4. Density functional theory results with the high-temperature structure at 315 K. (a) Total E as a function of ordered moment M_s on a Mn site for FM_b and $CAFM_a$. Squares indicate equilibrium positions. The ordered moment $M \approx 3.6$ μ_B agrees with the experimental value well. (b) Density of states in the PM phase. The inset of (a) shows the 1st Brillouin zone, with the Dirac line node along the Y-S direction indicated by a red line. Energy in (b) is measured from the Fermi level.

a ring of scattering emerges at AFM zone center positions such as (0 0 $\pm$ 1) and (0 $\pm$ 1 0). The diameter of the rings increases with increasing the E transfer [see Figs. 3(b) and 3(c)], indicative of dispersive spin waves. In sharp contrast, the magnetic excitations exhibit different features at 350 K. Diffuse magnetic excitations can be seen in Fig. 3(d) at around 5 meV due to the closure of the spin gap. As E transfer increases, the magnetic excitations become more diffuse and spread out without the ringlike feature, as shown in Fig. 3(e), and eventually evolve to be hardly visible at the high E transfer region in Fig. 3(f). This indicates the existence of the low-E AFM spin fluctuations at 350 K. It is worthwhile pointing out that we do not observe clear spin-wave branches associated with the FM ordered phase at 350 K, which is understood due to the low FM moment ≈0.41 μ_B [see inset of Fig. 1(b) and small mass of the coaligned crystals (≈600 mg)].

To quantitatively determine the magnetic interactions in $Sr_{1-y}Mn_{1-z}Sb_2$, we have performed linear spin wave calculations using the SpinW package [15] for the following spin Hamiltonian:

$$H = \sum_{i,j} J_{ij} \mathbf{S}_i \cdot \mathbf{S}_j + \sum_{\alpha,\beta,i} S_i^{\alpha} A_i^{\alpha\beta} S_i^{\beta}, \qquad (1)$$

where $\mathbf{S}_i$ is a spin operator, J_{ij} is an exchange coupling between spins, and $A_i^{\alpha\beta}$ is a 3×3 matrix representing the single-ion anisotropy. By fitting to the experimental magnon dispersions and intensities, we obtain the AFM nearest-neighbor (NN) $J_1 \approx 9.3(3)$ meV, interlayer FM $J_\perp \approx -0.26(8)$ meV, and anisotropy parameter $A_i = \mathrm{diag}(0, 0.12(5), 0.3(1))$. The interlayer $J_\perp$ is less than 2.8% of in-plane J_1, signaling the quasi-2D magnetism. The $J_\perp$ is considerably weaker than that proposed in Ref. [14] on $AMnBi_2$ (A=Ca,Sr) (with similar interlayer Mn-Mn distances), which was claimed as enhancement due to the Dirac carrier Bi layers. The emergence of the spin gap is ascribed to the uniaxial single-ion anisotropy.

To gain insight into the experimental observations, we performed DFT calculations for stoichiometric $SrMnSb_2$ using the high-temperature structure at 315 K and the low-temperature one at 5 K [3]. Using the 315 K structure, we compute the total E of several symmetry-allowed magnetic

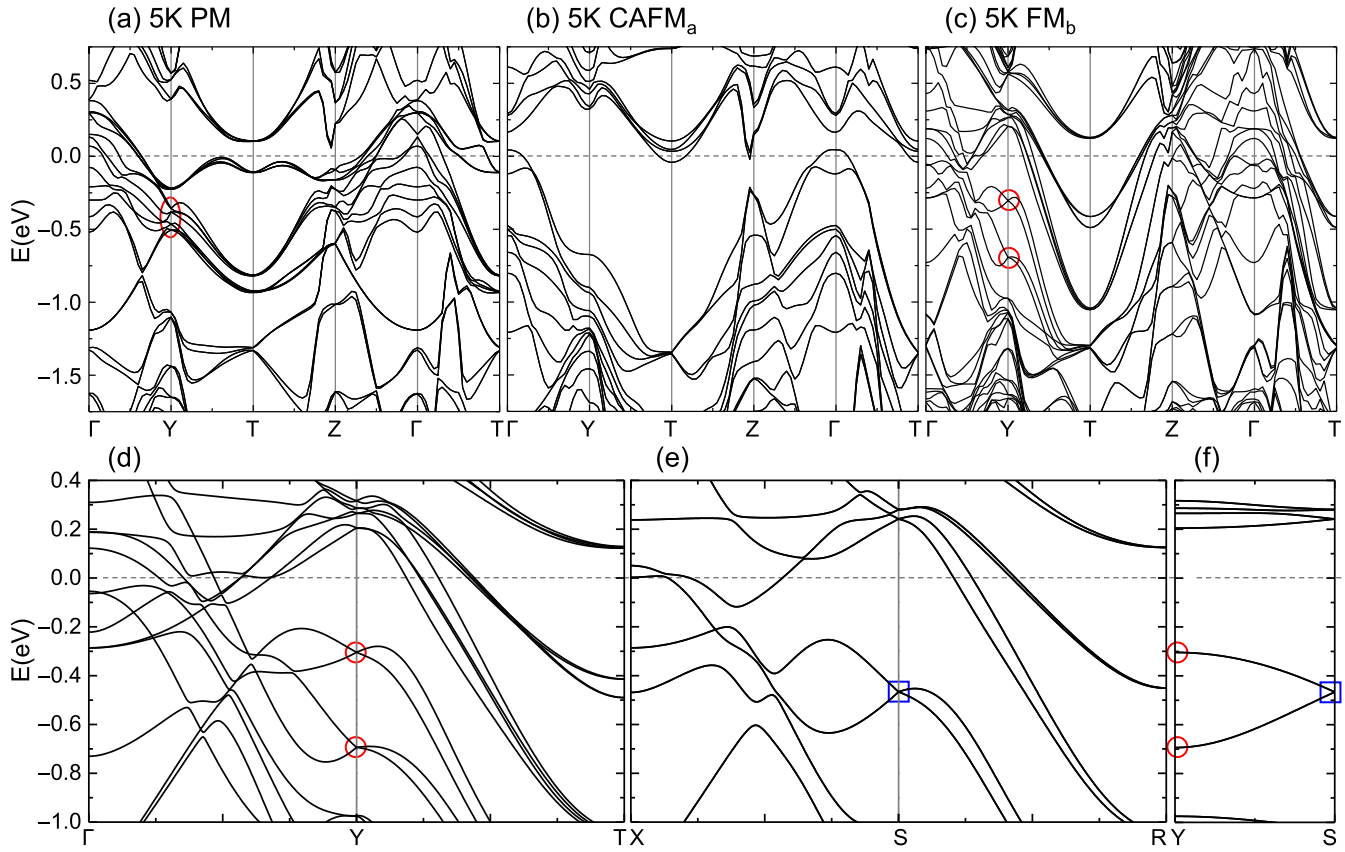

FIG. 5. Dispersion relation along high-symmetry lines for (a) PM, (b) CAFM$_a$, and (c) FM$_b$. The low-temperature structure at 5 K is used. Dirac dispersions are indicated by circles in (a) and (c). (d)–(f) are the magnified view of the Dirac dispersions in the FM$_b$ state along different directions, showing the evolution of two nondegenerate Dirac cones at the Y point (red circles) gets close with each other at the S point (blue squares). Energy is measured from the Fermi level.

configurations [3], including *C*-type AFM (CAFM), *G*-type AFM, *A*-type AFM, and FM with spin orientation taken along the *a*, *b*, or *c* axis (the spin orientation will be indicated as a subscript as, for example, CAFM$_a$). It turned out that CAFM$_a$ is most stable, while the FM$_b$ state is more stable than FM$_a$ and FM$_c$. However, constrained moment calculations show these compete depending on ordered Mn moment size M_s. As shown in Fig. 4(a), the relative E between FM$_b$ and CAFM$_a$ is reversed when the ordered Mn moment M_s is suppressed at around $M_s = 1.6\ \mu_B$. In the PM state ($M_s = 0$), the density of states (DOS) has a sharp peak near the Fermi level ($E = 0$) as shown in Fig. 4(b). Thus, the leading instability in the high-temperature PM phase is toward FM ordering due to the Stoner instability, followed by the first-order transition from FM$_b$ to CAFM$_a$ at lower temperature with much larger M_s ($\approx$3.6 μ_B at 5 K [3]). This provides a natural explanation for the sequence of magnetic transitions reported from experiments [3].

Using the 5 K structure, we computed the total E of several magnetic configurations and found that the CAFM$_a$ state remains the most stable magnetic ordering [the FM$_b$ is higher in energy by 325 meV per chemical formula (CF)]. The couplings and spin angular momentum we extract of $S^{\rm cal} = 1.8$ (1.89), $J_1^{\rm cal} = 25.0$ meV (9.3 meV), $J_\perp^{\rm cal} = -0.23$ meV (-0.26 meV), single-ion anisotropy $A_i^{\rm cal} = {\rm diag}(0, 0.16, 0.16)$ (diag(0, 0.12, 0.3)) from DFT (see more details in Ref. [22]) are of the same sign and similar magnitudes as extracted from neutron scattering (in brackets). For the theoretical model, the spin gap at the Γ point is expressed as $\sqrt{K^2(2S-1)^2 + 8J_1KS(2S-1)}$ [23]. Using DFT results, the spin gap is estimated to be 12.2 meV, which is close to the experimental observation of 8.5 meV. The consistency of the DFT calculations with the measured magnetic ordering, coupling strengths, and spin gap validates it for modeling the effects of magnetism.

To understand this further we examine the electronic band structures of the PM, the CAFM$_a$ and the FM$_b$ states, as shown in Figs. 5(a), 5(b) and 5(c), respectively. Because of the nonsymmorphic symmetry, Dirac cones are expected at the Y and the T points [5,24] (X and M points in the notation of Ref. [5]). In the PM state, the Dirac cones are indeed observed at $E \sim -0.5$ eV at the Y point and at $E \sim -1.3$ eV at the T point. The band structure is influenced by magnetic order rather strongly. In the CAFM$_a$ state, no clear Dirac cones are observed at the Y point in this E window although the Dirac cone at the T point remains at $E \sim -1.3$ eV. This dispersion relation shows some similarities to that using GAFM$_a$ [6]. As discussed in Refs. [5,6], the location of the Dirac cone is too far from the Fermi level to account for the π Berry phase reported in Ref. [3]. A small canting of 6° in the previously

proposed AFM order in Fig. 1(a) cannot be responsible for it either. We note that previous DFT calculations [7] have discussed one possibility of observing the nontrivial Berry phase in the canted $CAFM_a$ phase by raising the Fermi energy so that the gapped Dirac bands at the Y point, corresponding to our Z point in Fig. 5(b), are more populated by electrons. This picture appears to be in contradiction to Sr and Mn deficiencies, corresponding to hole doping. The coupling between the Dirac electron behavior and magnetism observed in previous experiments [3] cannot be understood in this scenario either. Interestingly, we found when the FM_b state is considered, the Dirac cone appearing in the PM state at the Y point splits due to the spin polarization, and one of them could be closer to the Fermi level depending on the size of the FM moment [for instance $E \sim -0.3$ eV in Fig. 5(c)]. As shown in Figs. 5(d)–5(f), these Dirac cones form a line node along the Y-S direction and become nearly degenerate at the S point as a consequence of two units of $MnSb(2)_4$ and Sb(1) layers, each of which supports two-dimensional Dirac cones, and the mixing between the two units is suppressed at $k_x = \pi/a$.

Once the Fermi level is tuned near the Dirac cones, the π Berry phase should be manifested in the quantum oscillations of magnetoresistance or magnetization. A natural question is how one can realize this condition in $SrMnSb_2$. In reality, the π Berry phase is observed only in nonstoichiometric $Sr_{1-y}Mn_{1-z}Sb_2$ samples in Ref. [3]. Thus, the current study suggests the following scenario. The relative energy between the $CAFM_a$ and FM_b in nonstoichiometric samples could be much smaller than that in stoichiometric samples. As a result, the FM_b state could remain in place more easily at low temperatures, leading to a likely phase separation between collinear AFM_a and FM_b phases. Our DFT calculations show $\approx$1 electron/CF needs to be removed to align the Fermi level and the Dirac points. While this is larger than the Sr and Mn off stoichiometries (0.2 electrons/CF with $y + z \sim 0.1$), the Dirac points are expected to become closer to the Fermi level once correlation effects are better treated, especially on Mn d states. This supports the scenario of two-phase coexistence because FM_b regions should have fewer electrons. According to the experimental saturation magnetization $\approx$0.45 μ_B at 5 K and the theoretical moment $2S = 3.6$ μ_B, the FM phase occupies $\approx$12% in the nonstoichiometric $Sr_{1-y}Mn_{1-z}Sb_2$. Such FM order could split the Dirac point into two and shift one of them closer to the Fermi level. Moreover, the Fermi level is expected to shift further by Sr and/or Mn off stoichiometries to be located in proximity to the Dirac cones to induce the π Berry phase.

Would there exist Weyl points in the FM_b phase as the time-reversal symmetry is broken in $Sr_{1-y}Mn_{1-z}Sb_2$? In fact, Weyl points do exist when the ordered moment M_s is small as schematically shown in Figs. 6(a)–6(c). There are only Dirac points in the paramagnetic state in Fig. 6(a). A small moment of $M_s = 0.09$ μ_B drives Weyl points to form at $\mathbf{k} = (0, \pi/b, \pm\delta\pi/c)$ with $\delta = 0.0631$ [see (Fig. 6(b)]. Two Weyl points with the same energy reside at different points in momentum space here, consistent with the recent reports on other compounds [25,26], showing the universal feature of Weyl fermions driven by the time-reversal symmetry breaking. Interestingly, with increasing M_s, these two Weyl

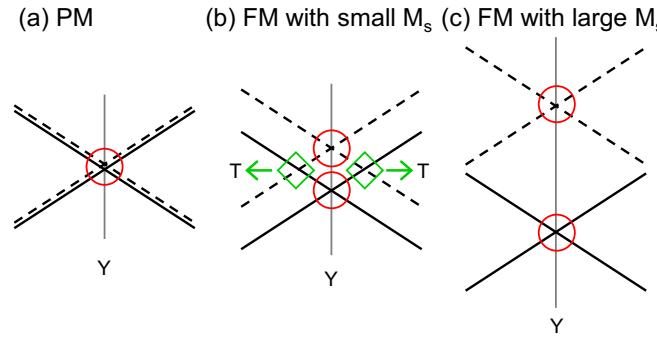

FIG. 6. The schematic evolution of Dirac and Weyl dispersions with the FM_b ordering. Solid (broken) lines are mainly from majority (minority) spin electrons. With small M_s, Weyl cones emerge between the Y and the T points as indicated by diamonds (b).

points move toward the T point and eventually pair annihilate [see (Fig. 6(c)]. This pair annihilation however is hard to detect because of the band overlap. Thus, the novel feature of $Sr_{1-y}Mn_{1-z}Sb_2$ is that Dirac and Weyl dispersions could coexist in the weak FM_b moment and no Weyl dispersions are formed with higher FM_b moment. This is related to the nonsymmorphic symmetry of space group *Pnma* that protects the twofold (fourfold) band degeneracy in the FM_b (PM) phase along the Y-S direction, i.e., spin-polarized (unpolarized) Dirac dispersions are stable [27].

To elucidate this, we provide the detailed information of the density functional theory calculations regarding the evolution of Dirac dispersions in the FM_b phase with increasing the ordered moment M_s. Because of the Dirac dispersions in the PM phase [Fig. 5(a)], Weyl dispersions are expected to emerge by breaking the time-reversal symmetry. By the FM_b ordering, majority spin and minority spin bands split, resulting in the degeneracy lifting in the Dirac dispersions. As shown in Fig. 7(a), there remains a band crossing along the Y-T line when the ordered moment M_s is small. However, because of the overlap of many bands, such a band crossing is hard to detect when M_s is increased as shown in Fig. 7(b). The location of the band crossing in the first octant of the Brillouin zone is indicated in Fig. 7(c). This band crossing corresponds to a Weyl point.

The band dispersions in the red box in Fig. 7(a) are magnified in Fig. 7(d), which confirms the splitting of the Dirac dispersion at the Y point, leaving a band crossing along the Y-T direction. As shown in Fig. 7(e), the twofold degeneracy of each Dirac cone remains along the Y-S direction. In fact, this degeneracy is protected by the nonsymmorphic symmetry of space group *Pnma* (No. 62) [25]. The gap between the two twofold degenerate points remains finite at the S point, $\approx$0.05 meV within the current DFT, because there is no symmetry reason to guarantee the degeneracy between them. The role of the time-reversal symmetry breaking in the FM_b phase is merely reducing the degeneracy of Dirac points from 4 to 2. Because of the quasi-two-dimensional nature, velocity $\mathbf{v}$ at the Weyl point is highly anisotropic, $v_c > v_b \gg v_a$, and the dispersion along the a direction is almost quadratic in the energy scales used in Fig. 7 [compare the slope in (d), (f), and (g)].

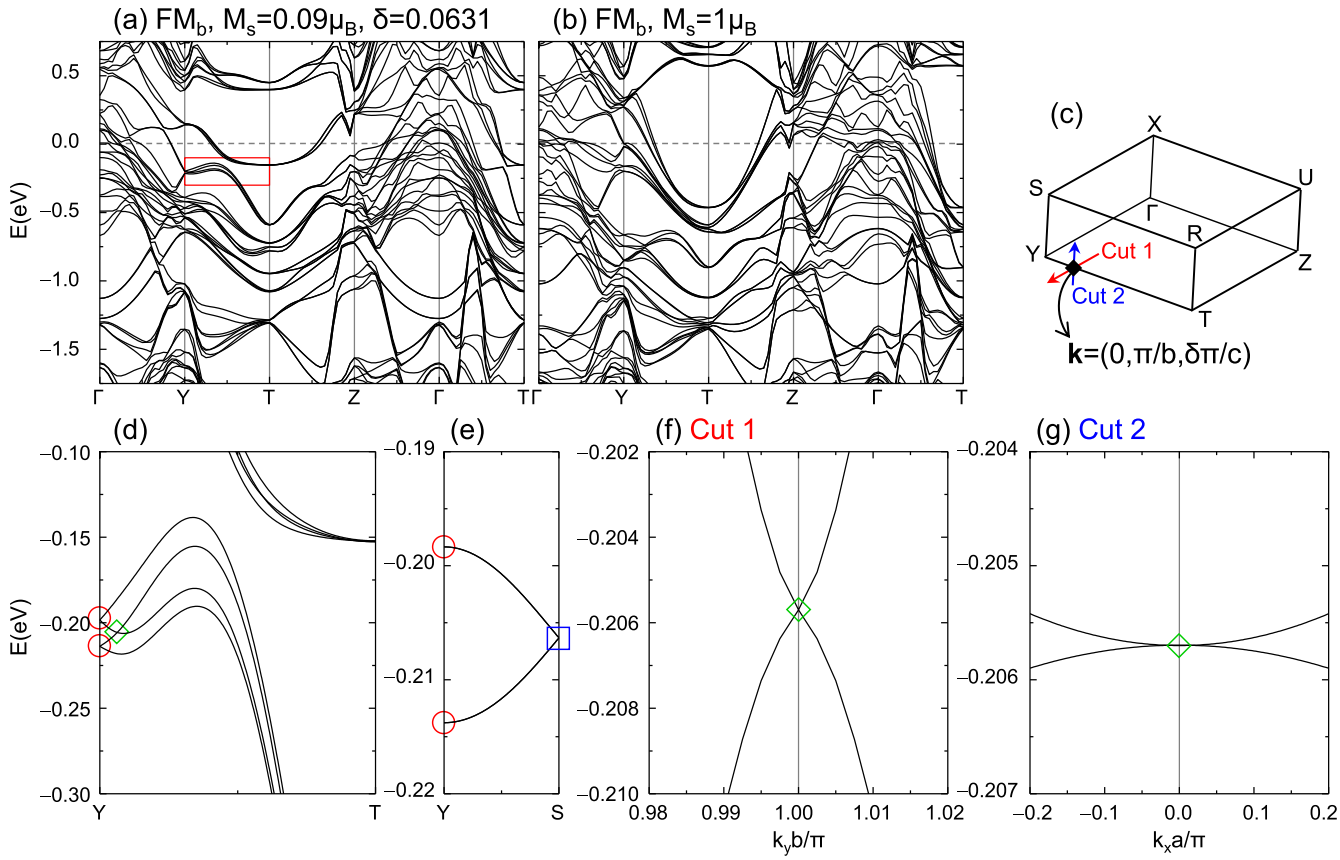

FIG. 7. Density functional theory results for the evolution of Dirac and Weyl dispersions. Dispersion relation for the FM$_b$ phase with $M_s = 0.09\ \mu_B$ (a) and $M_s = 1\ \mu_B$ (b). In (a), Weyl dispersion is seen inside the red box. The location of Weyl point $\mathbf{k} = (0, \pi/b, \delta\pi/c)$ in the first octant of the Brillouin zone is indicated in (c). Another Weyl point is located at $\mathbf{k} = (0, \pi/b, -\delta\pi/c)$. With $M_s = 1\ \mu_B$, such Weyl dispersion is hard to detect in (b). The dispersions in the red box in (a) are magnified in (d). (e) The evolution of two Dirac line nodes along the Y-S line. Two Dirac points get extremely close at the S point as indicated by a blue square. (f) and (g) different cuts across the Weyl point at $\mathbf{k} = (0, \pi/b, \delta\pi/c)$ with $\delta = 0.0631$ for the FM$_b$ phase with $M_s = 0.09\ \mu_B$. In (d)–(g), Dirac points and Weyl points are indicated by red circles and green diamonds, respectively. Energy is measured from the Fermi level.

With increasing M_s, the splitting between majority spin bands and minority spin bands is increased. The Weyl points are shifted toward the T point by this and eventually pair annihilate there [see (Fig. 6(c)]. However, even with relatively small M_s, it becomes hard to observe Weyl points because of the overlap with the other bands. When the FM$_b$ ordering is fully developed, Dirac dispersions from minority spin electrons are above the Fermi level and do not have overlap with Dirac dispersions from majority spin electrons. Thus, no Weyl dispersions are formed as shown in Fig. 5(c).

IV. CONCLUSION

In summary, we have examined the magnetic excitations and investigated the origin of the Dirac semimetallic behavior in nonstoichiometric $Sr_{1-y}Mn_{1-z}Sb_2$. The magnetic exchange constants are determined, indicative of a quasi-2D magnetism, with no significant enhancement of $J_\perp$ by the Dirac carrier Sb layers. The constrained magnetization calculations by our DFT interpreted the occurrence of the successive PM-FM-AFM transition. We further demonstrate that the FM order plays an important role in realizing the Dirac points near the Fermi level whereas various AFM orders have a disfavoring effect on it in $Sr_{1-y}Mn_{1-z}Sb_2$. The magnitude of FM moment is also found to influence the Weyl dispersion significantly, leading to the coexistence of Dirac and Weyl dispersions at low moment and sole Dirac dispersion at a higher moment. Our study provides a clue to the understanding of the origin of Dirac semimetals and to seek for Dirac/Weyl semimetals by adjusting the magnetic order.

ACKNOWLEDGMENTS

Primary support for this study came from the U.S. Department of Energy under EPSCoR Grant No. DESC0012432, with additional support from the Louisiana Board of Regents. A portion of this research used resources at Spallation Neutron Source, a DOE Office of Science User Facility operated by the Oak Ridge National Laboratory. The research by SO and DAT was sponsored by the Laboratory Directed Research and Development Program (LDRD) of Oak Ridge National Laboratory, managed by UT-Battelle, LLC, for the U.S. Department of Energy.

This manuscript has been partially supported by UT-Battelle, LLC under Contract No. DE-AC05-00OR22725 with the U.S. Department of Energy. The United States

[1] K. S. Novoselov, A. K. Geim, S. V. Morozov, D. Jiang, M. I. Katsnelson, I. V. Grigorieva, S. V. Dubosnos, and A. A. Firsov, Nature (London) **438**, 197 (2005).

[2] N. P. Armitage, E. J. Mele, and A. Vishwanath, Rev. Mod. Phys. **90**, 015001 (2018).

[3] J. Y. Liu, J. Hu, Q. Zhang, D. Graf, H. B. Cao, S. M. A. Radmanesh, D. J. Adams, Y. L. Zhu, G. F. Cheng, X. Liu, W. A. Phelan, J. Wei, M. Jaime, F. Balakirev, D. A. Tennant, J. F. DiTusa, I. Chiorescu, L. Spinu, and Z. Q. Mao, Nat. Mater. **16**, 905 (2017).

[4] C. P. Weber, B. S. Berggren, M. G. Masten, T. C. Ogloza, S. Deckoff-Jones, J. Madéo, M. K. L. Man, K. M. Dani, L. Zhao, G. Chen, J. Liu, Z. Mao, L. M. Schoop, B. V. Lotsch, S. S. P. Parkin, and M. Ali, J. Appl. Phys. **122**, 223102 (2017).

[5] S. V. Ramankutty, J. Henke, A. Schiphorst, R. Nutakki, S. Bron, G. Araizi-Kanoutas, S. K. Mishra, Lei Li, Y. K. Huang, T. K. Kim, M. Hoesch, C. Schlueter, T.-L. Lee, A. de Visser, Zhicheng Zhong, Jasper van Wezel, E. van Heumen, and M. S. Golden, SciPost Phys. **4**, 010 (2018).

[6] M. A. Farhan, G. Lee, and J. H. Shim, J. Phys.: Condens. Matter **26**, 042201 (2014).

[7] J. S. You, I. Lee, E. S. Choi, Y. J. Jo, J. H. Shim, and J. S. Kim, Curr. Appl. Phys. **19**, 230 (2018).

[8] M. C. Rahn, A. J. Princep, A. Piovano, J. Kulda, Y. F. Guo, Y. G. Shi, and A. T. Boothroyd, Phys. Rev. B **95**, 134405 (2017).

[9] J. K. Wang, L. L. Zhao, Q. Yin, G. Kotliar, M. S. Kim, M. C. Aronson, and E. Morosan, Phys. Rev. B **84**, 064428 (2011).

[10] S. J. Ray and L. Alff, Phys. Status Solidi B **254**, 1600163 (2017).

[11] S. Huang, J. Kim, W. A. Shelton, E. W. Plummer, and R. Jin, PNAS **114**, 6256 (2017).

[12] J. Liu, J. Hu, H. Cao, Y. Zhu, A. Chuang, D. Graf, D. J. Adams, S. M. A. Radmanesh, L. Spinu, I. Chiorescu, and Z. Mao, Sci. Rep. **6**, 30525 (2016).

[13] Y. F. Guo, A. J. Princep, X. Zhang, P. Manuel, D. Khalyavin, I. I. Mazin, Y. G. Shi, and A. T. Boothroyd, Phys. Rev. B **90**, 075120 (2014).

[14] A. Zhang, C. Liu, C. Yi, G. Zhao, T. Xia, J. Ji, Y. Shi, R. Yu, X. Wang, C. Chen, and Q. Zhang, Nat. Commun. **7**, 13833 (2015).

[15] S. Toth and B. Lake, J. Phys.: Condens. Matter **27**, 166002 (2015).

[16] P. E. Blöchl, Phys. Rev. B **50**, 17953 (1994).

[17] G. Kresse and J. Furthmüller, Phys. Rev. B **54**, 11169 (1996).

[18] G. Kresse and D. Joubert, Phys. Rev. B **59**, 1758 (1999).

[19] A. Taroni, S. T. Bramwell, and P. C. W. Holdsworth, J. Phys.: Condens. Matter **20**, 275233 (2008).

[20] Q. Zhang, C. M. N. Kumar, W. Tian, K. W. Dennis, A. I. Goldman, and D. Vaknin, Phys. Rev. B **93**, 094413 (2016).

[21] Q. Zhang, W. Tian, S. G. Peterson, K. W. Dennis, and D. Vaknin, Phys. Rev. B **91**, 064418 (2015).

[22] By mapping the total energy of different magnetic ordering to that of a Heisenberg-type model, we extract these parameters. The precise values of these parameters depend on the value of local U on a Mn site and the exchange correlation potential, which could reconcile why these values are larger than those obtained from the fits to experimental spin waves.

[23] T. Holstein and H. Primakoff, Phys. Rev. **58**, 1098 (1940).

[24] S. M. Young and C. L. Kane, Phys. Rev. Lett. **115**, 126803 (2015).

[25] A. K. Mitchell and L. Fritz, Phys. Rev. B **92**, 121109(R) (2015).

[26] H.-R. Chang, J. Zhou, S.-X. Wang, W.-Y. Shan, and D. Xiao, Phys. Rev. B **92**, 241103(R) (2015).

[27] B. Bradlyn, L. Elcoro, J. Cano, M. G. Vergniory, Z. Wang, C. Felser, M. I. Aroyo, and B. A. Bernevig, Nature (London) **547**, 298 (2017).

[28] http://energy.gov/downloads/doe-public-access-plan